Realization of Band Convergence in p-Type TiCoSb Half-Heusler Alloy Significantly Enhances the Thermoelectric Performance

Ajay Kumar Verma, Kishor Kumar Johari, Paritosh Dubey, Durgesh Kumar Sharma, Sudhir Kumar, Sanjay Rangnate Dhakate, Christophe Candolfi, Bertrand Lenoir, Bhasker Gahtori

Realization of Band Convergence in p-Type TiCoSb Half-Heusler Alloy Significantly Enhances the Thermoelectric Performance

Ajay Kumar Verma[1, 2, 3, 4], Kishor Kumar Johari[1, 2], Paritosh Dubey[2, 5], Durgesh Kumar Sharma[6,7], Sudhir Kumar[7], Sanjay Rangnate Dhakate [1, 2], Christophe Candolfi[8], Bertrand Lenoir[8 *], and Bhasker Gahtori[1, 2, *]

[1]*CSIR-National Physical Laboratory, Dr. K.S. Krishnan Marg, New Delhi 110012, India*
[2]*Academy of Scientific & Innovative Research (AcSIR), Ghaziabad, 201002, India*
[3]*Functional Materials and Microsystems Research Group and the Micro Nano Research Facility, RMIT University, Melbourne, VIC 3001, Australia*
[4]*School of Engineering, RMIT University, GPO Box 2476, Melbourne, Victoria 3001, Australia*
[5]*CSIR-National Metallurgical Laboratory, Jamshedpur 831007, India*
[6]*Present Address: Theoretical Sciences Unit, Jawaharlal Nehru Centre for Advanced Scientific Research, Jakkur, Bangalore - 560064, India.*
[7]*Applied Physics Department, Faculty of Engineering and Technology, M. J. P. Rohilkhand University, Bareilly - 243006, India*
[8]*Institut Jean Lamour UMR 7198 CNRS – Université de Lorraine Campus ARTEM, 2 allée André Guinier, BP 50840, Nancy 54011, France*

Abstract

Band engineering is a promising approach that proved successful in enhancing the thermoelectric performance of several families of thermoelectric materials. Here, we show how this mechanism can be induced in the *p*-type TiCoSb half-Heusler (HH) compound to effectively improve the Seebeck coefficient. Both the Pisarenko plot and electronic band structure calculations demonstrate that this enhancement is due to increased density-of-states effective mass resulting from the convergence of two valence band maxima. Our calculations evidence that the valence band maximum of TiCoSb lying at the Γ point exhibits a small energy difference of 51 meV with respect to the valence band edge at the L point. Experimentally, this energy offset can be tuned by both Fe and Sn substitutions on the Co and Sb site, respectively. An Sn doping level as low as x = 0.03 is sufficient to drive more than ~ 100 % increase in the power factor at room temperature.

*Corresponding authors: bhasker@nplindia.org, bertrand.lenoir@univ-lorraine.fr
Tel.: +91-11-45608556; Fax: +91-11-45609310

Further, defects at various length-scales, that include point defects, edge dislocations and nano-sized grains evidenced by electron microscopy (FESEM and HRTEM), results in enhanced phonon scattering which substantially reduces the lattice thermal conductivity to ~ 4.2 W m^{-1} K^{-1} at 873 K. Combined with enhanced power factor, a peak *ZT* value of ~ 0.4 was achieved at 873 K in $TiCo_{0.85}Fe_{0.15}Sb_{0.97}Sn_{0.03}$. In addition, the micro-hardness and fracture toughness were found to be enhanced for all the synthesized samples, falling in the range of 8.3 – 8.6 GPa and 1.8 – 2 MPa-$m^{-1/2}$, respectively. Our results highlight how the combination of band convergence and microstructure engineering in the HH alloy TiCoSb is effective for tuning its thermoelectric performance.

Keywords: Thermoelectric, half-Heusler, band convergence, weighted mobility, micro-hardness

1. Introduction

Thermoelectric technology have stirred up strong interest due to its ability to directly transform waste heat into electricity or to cool down electronic devices[1]. The performance of a thermoelectric material is defined by the dimensionless thermoelectric figure of merit $ZT = \frac{\alpha^2 \sigma T}{\kappa_L + \kappa_e}$, where α is Seebeck coefficient (or thermopower), σ is the electrical conductivity, *T* is the absolute temperature, κ_L is the lattice thermal conductivity and κ_e is the electronic thermal conductivity. Enhancing the power factor $\alpha^2\sigma$ and lowering the total thermal conductivity $\kappa = \kappa_L + \kappa_e$ are the two leading strategies for improving the *ZT* values. Several approaches such as band structure engineering [2], nano-structuring [3] or modulation doping [4, 5] have been explored for enhancing the TE performance and overcoming the strong interdependence of these three transport coefficients.

Several families of TE materials have been investigated over the last decades for power generation applications at high temperatures such as chalcogenides [6], skutterudites [7], silicides [8] and clathrates [9]. Among them, half-Heuslers (HH) [3, 10, 11] are promising compounds for mid- to high-temperature applications due to their excellent mechanical robustness, high thermal stability, environmentally-friendly and low-cost constituting elements in addition to their good TE performance [3, 10-12]. HH compounds crystallize in the cubic MgAgAs structure type described in the $F\bar{4}3m$ space group (space group no. 216). The face-centred cubic (fcc) lattice can be viewed as three interpenetrated sub-lattices of equal unit cell size [13, 14]. This family offers a wide range of chemical compositions, even though compounds with 18 valence electron count (VEC) are the most promising for thermoelectric applications due to their narrow band gap and sharp slope in the density of states near the Fermi level [15, 16]. Among HH compounds, *X*NiSn and *X*CoSb (*X* = Ti, Zr, Hf) have been widely explored, notably leading to *n*-type compositions (with *X* = Zr) with high thermoelectric performance. [10-14, 16-20] In comparison, *p*-type analogues based on TiCoSb exhibit lower TE performance despite various approaches employed such as doping [14, 16-19], nano structuring [21] and nano-composite [22].

Among the band engineering tools used to advantageously modify the valence or conduction band manifold, band convergence provides an effective mean to increase the Seebeck coefficient. α is proportional to the density-of-state effective mass $m_{DOS}^* = (N_v)^{2/3} m_b^*$ [23, 24], where N_v is the number of valleys (band extrema) of the conducting bands, which includes orbital degeneracy, and m_b^* is the single valley band effective mass that includes spin degeneracy [25]. Therefore, m_{DOS}^* can be increased either by increasing N_v and/or m_b^*. While m_b^* can be increased by distortion of the DOS through band flattening or resonant levels [26], N_v mainly depends on the crystal structure symmetry and can be increased by band convergence of several band extrema

offset by an energy difference of few k_BT [24, 27]. These multiple degenerate valleys improve the m^*_{DOS} without adversely impacting the mobility of the charge carriers, provided that intervalley scattering is not strong [24]. Band convergence may easily occur in materials with a highly-symmetric crystal structure and Fermi surface forming isolated pockets at low symmetry points [24, 28]. This effect has been successfully induced in many systems such as $CoSb_3$ [29], Mg_2Si [30], SnTe [28, 31, 32], InSe [33], Bi_2Te_3[34, 35], PbTe [36, 37], and half-Heuslers [38-41]. In the *p*-type HH compound TiCoSb, angle-resolved photoemission spectroscopy (ARPES) measurements on single crystals have evidenced the presence of several valence bands at the L and Γ points of the Brillouin zone with a very small energy offset of ~ 0.05eV [40]. These results suggest that convergence of these bands may be achieved upon appropriate substitutions, thereby providing a straightforward mean to enhance the TE performance of this compound.

In this study, we demonstrate how convergence of the valence bands can be experimentally realized in TiCoSb by co-substitutions of Fe and Sn on the Co and Sb site, respectively. The choice of Fe is motivated by previous study [16], demonstrating that substituting Fe for Co effectively switches the *n*-type nature of pure polycrystalline TiCoSb into *p*-type, with 15% being the concentration at which the highest TE performance are achieved. While Fe shifts the Fermi level deeper into the valence bands to ensure *p*-type electrical properties in agreement with these results, substituting Sn for Sb (0 – 4 %) further promotes band convergence, ultimately leading to enhanced TE performance. Furthermore, a substantial reduction in the lattice thermal conductivity is realized due to the scattering of heat carrying phonons from defects at various length scales such as point defects, edge dislocations and nano-sized grains, observed by electron microscopy. Thus, a peak *ZT* of ~0.4 at 873 K was achieved for the composition $TiCo_{0.85}Fe_{0.15}Sb_{0.97}Sn_{0.03}$, which corresponds to a ~110 % improvement with respect to $TiCo_{0.85}Fe_{0.15}Sb$.

2. Experimental and computational details

To synthesize the samples with composition $TiCo_{0.85}Fe_{0.15}Sb_{1-x}Sn_x$ ($x = 0 - 0.04$), high-purity Ti granules (99.9 %), Co pieces (99.9 %), Sb shots (99.9999 %) Fe granules (99.98 %) and Sn shots (99.999%), all purchased from Alfa Aesar, were weighed in stoichiometric proportions. Arc melting was performed by using an arc-melter (Edmund Bühler GmbH, MAM-1) under an inert argon atmosphere. The arc-melted ingots were flipped and remelted several times for chemical homogenization. Arc-melted ingots were successively pulverized into fine powders by using a mortar pestle. The pulverized powders were packed into a graphite die of 12.7 mm diameter and consolidated employing spark plasma sintering (Dr. Sinter, 725) at 1373 K under a uniaxial pressure of 50 MPa. The density of all the samples was measured using a system based on the Archimedes principle (Mettler Toledo, model ML204/A01). With no exceptions, all the samples show a density close to the theoretical density determined from X-ray diffraction data and their relative density are given in in Table S-1 in the *Supporting Information* (*SI*).

Powder X-ray diffraction (PXRD) patterns were obtained using an X-ray diffractometer (Rigaku Miniflex II). Rietveld refinements against XRD data were carried out using FullProf software [42]. Analysis of the surface morphology along with energy-dispersive spectroscopy (EDS; EDAX OCTANE ELECT SUPER) was accomplished using a field emission scanning electron microscope (FESEM; TESCAN MAGNA GMH). The microstructure of the sample was further investigated through transmission electron microscopy (JEOL JEM 2200 FS TEM), with an applied acceleration voltage of 200 keV. The detailed HRTEM analysis has been done by using the GATAN Digital Micrograph software. The temperature-dependent electrical resistivity and Seebeck coefficient were measured from room temperature (RT) to 873 K using a ZEM-3 system (ULVAC-RIKO). A Hall effect measurement system (HEMS, Nanomagnetics) was utilized to

determine the room-temperature Hall carrier concentration together with their Hall mobility. The temperature dependent thermal conductivity of the samples was determined from the measured specific heat (DSC-NETZSCH, 404 F3) and thermal diffusivity (LFA).

In addition, we have performed theoretical analysis based on density functional theory (DFT) as implemented in Vienna Ab-initio Simulation Package (VASP). It incorporates projected augmented wave scheme to calculate pseudo potential of elements. The Perdew-Burke-Ernzerhof (PBE) form of generalized gradient approximation (GGA) was considered for the electron exchange correlation functional. For the expansion of plane wave basis sets, we used a 500eV kinetic energy cut-off with a Γ-centered, 4×4×4 mesh of *k*-points. The integration within the first Brillouin zone (BZ) was carried out using Gaussian smearing method with a smearing width of 0.10 eV. We opted energy convergence criteria of 10^{-6} eV in all set of calculations. Before performing any calculations, the atomic positions have been relaxed so that the Hellman-Feynman force on atoms was ≤ 0.02 eV/Å. The unit cell size, consisting of one atom of each Ti, Co, and Sb, was multiplied by 3×3×3 there after 4 Fe atoms at Co sites introduced, resulting in a Fe concentration of 0.148 (in fraction). A single atom of Sn was substituted at the Sb site (concentration of 0.037) in Fe-substituted TiCoSb. The electron effective masses were derived from a fit (second order) of the energy dispersion curves near the band extrema.

3. Results and discussion

3.1. Structural analysis

To confirm the phase purity of synthesized samples, X-ray diffraction (XRD) was performed for all the samples $TiCo_{0.85}Fe_{0.15}Sb_{1-x}Sn_x$ ($0 \leq x \leq 0.04$). The data, presented in Fig. 1(a), show that all the peaks are well indexed with the cubic TiCoSb HH phase (PDF Card No. 00-030-0083). Further, no significant shift in the peaks upon Sn doping in $TiCo_{0.85}Fe_{0.15}Sb$ is observed. The

Rietveld refinement of the XRD pattern of the representative sample $TiCo_{0.85}Fe_{0.15}Sb_{0.97}Sn_{0.03}$ (Fig. 1(b)) shows the good agreement between the experimental and predicted patterns. The Rietveld refinement parameters of all the samples are gathered in *Supporting Information (SI)* as Table S-1. The practically unchanged lattice parameters in the Sn-containing samples can be attributed to the comparable atomic radii of Sb = 139 pm and Sn = 142 pm[43].

The surface morphology and elemental compositions of the representative sample $TiCo_{0.85}Fe_{0.15}Sb_{0.97}Sn_{0.03}$ were investigated by field emission scanning electron microscopy (FESEM) and energy dispersive X-ray spectroscopy (EDS), shown in Fig. 2. The FESEM image of fractured surface shown in Fig. 2(a) confirms the high densification of the sample due to the absence of visible pores, which is further confirmed by the higher-resolution FESEM image (Fig. 2(b)) of the polished surface (see Table S-1 in the SI where the experimental densities of the samples are listed). The matrix (Fig. 2(c)) exhibits an actual chemical composition very close to the nominal one as evidenced by the EDS spectra (Fig. 2(d)). The very small regions of dark contrast are of in-situ grown secondary phases (Fig. 2(e)), identified as a Ti-rich secondary phase based on EDS analysis (Fig. 2(f)).

To further investigate the microstructure, high resolution transmission electron microscope (HRTEM) analysis of the sample $TiCo_{0.85}Fe_{0.15}Sb_{0.97}Sn_{0.03}$ has been carried out (Fig. 3). Lattice planes are clearly visible and their calculated interplanar spacing agrees very well with that of the TiCoSb HH phase. The region R1 was analyzed by applying the Fast Fourier Transformation (FFT) followed by Inverse Fast Fourier Transformation (IFFT), illustrated in the inset of Fig. 3(a). The region R1 consists of two kinds of planes that correspond to (311) and (400) of the HH phase with a calculated *d*-spacing of 0.190 nm and 0.142 nm, respectively. Furthermore, the region R2 exhibits edge dislocation defects, clearly visible in the associated image processed via FFT

followed by IFFT of the selected area of the region R2. The selected area electron diffraction (SAED) pattern, corresponding to the region shown in Fig. 3(a) for the synthesized sample $TiCo_{0.85}Fe_{0.15}Sb_{0.97}Sn_{0.03}$ (Fig. 3(b)), evidences the superimposition of bright spots with Debye rings confirming its polycrystalline nature [44]. The diffraction pattern reflects the cubic crystal structure of the HH phase in the reciprocal space for which the Debye rings are found to correspond to *d*-spacings of 0.334, 0.281, 0.204, 0.173, 0.162, 0.142, 0.13, 0.118, and 0.102 nm. All of them are very close to those of the family of planes of the TiCoSb HH phase (111), (200), (220), (311), (222), (400), (420), (422), and (511), respectively.

3.2. Thermoelectric Properties

Fig. 4 shows the temperature-dependent electronic transport properties of all the synthesized samples $TiCo_{0.85}Fe_{0.15}Sb_{1-x}Sn_x$ ($0 \leq x \leq 0.04$). At room temperature, the Seebeck coefficient (α) increases monotonically with *x* up to 0.03, an upper limit above which a reverse trend is observed (Fig. 4(a)). To better understand this behavior, the theoretical Ioffe-Pisarenko curve has been calculated by a single-parabolic band (SPB) model with acoustic phonon scattering that was shown to dominate the transport in single crystals [40] according to the following relation [45, 46]

$$S = \frac{k_B}{e}\left(\frac{2F_1(\eta)}{F_0(\eta)} - \eta\right)$$

where the Fermi integral of order *j* is defined as $F_j(\eta) = \int_0^\infty \frac{\epsilon^j d\epsilon}{1+exp(\epsilon-\eta)}$. The chemical carrier concentration is expressed as $n = 4\pi\left(\frac{2m^*_{DOS}k_BT}{h^2}\right)^{\frac{3}{2}} F_{\frac{1}{2}}(\eta)$, while the Hall carrier concentration is given by $n_H = \frac{n}{r_H}$, with the Hall factor $r_H = \frac{3}{2}F_{1/2}(\eta)\frac{F_{-1/2}(\eta)}{2F_0^2(\eta)}$. In these expressions, η is the reduced chemical potential, ϵ is the reduced energy, k_B is the Boltzmann constant, e is the bare

electronic charge, m^*_{DOS} is the density-of-states effective mass, T is the temperature, and h is the Planck constant. The Ioffe-Pisarenko plot (Fig. 4(b)) shows that m^*_{DOS} increases with increasing the Sn content up to x = 0.03, with each sample following a distinct curve. The highest value of ~ $4m_e$ agrees with that determined from the Seebeck coefficient in single-crystalline TiCoSb, which has been taken as an indication of the convergence of the valence bands at the Γ and L points [40]. Further increasing the Sn content to x = 0.04 lowers α from 164 to ~ 142 μV K^{-1} at RT. This reduction might be attributed to the rise in energy separation between the above-mentioned valence bands. Furthermore, α increases with increasing temperature for all samples up to ~700 K. Above this temperature, α tends to level off for all Sn doped samples which is likely due to the onset of thermal activation of minority carriers across the electronic band gap. The α at elevated temperature may change by varying the band effective mass, mobility and concentration of both majority and minority carrier. The decrease in α at high temperature for x = 0.01 is faster than other samples may be owing to weak band convergence and it is dependent on temperature[47]. To better understand this behavior, we linearly fit the Seebeck coefficient at elevated temperature as shown in Fig. S-1(a) (*Supporting Information*), corresponding Seebeck gradient with temperature (dα/dT) is shown in Fig. S-1(b), wherein the increase in dα/dT with Sn up to 3% is likely due to rise in strength of band convergence. A maximum α value of ~ 248.5 μV K^{-1} is achieved in the x = 0.03 sample at ~ 825 K. Fig. 4(c) shows that the variations in α are highly dependent on the density-of-states effective mass and confirms that 3 at.% of Sn optimizes the band convergence in $TiCo_{0.85}Fe_{0.15}Sb$. Fig. 4(d) displays the temperature dependence of the electrical conductivity (σ) for all the samples $TiCo_{0.85}Fe_{0.15}Sb_{1-x}Sn_x$ ($0 \leq x \leq 0.04$). With no exception, σ increases with increasing temperature, indicative of a semiconducting behavior with a maximum value of 3.2×10^4 S m^{-1} achieved in $TiCo_{0.85}Fe_{0.15}Sb_{0.97}Sn_{0.03}$ at 874 K. σ increases

monotonically with increasing the Sn content up to x = 0.03 and shows no significant change beyond this value. The monotonic enhancement in σ with Sn doping can be ascribed to the convergence of the valence bands that tends to increase the charge carrier density without significantly deteriorating their mobility. This is in stark contrast with resonant levels that induce a pronounced drop in the charge carrier mobility due to resonant scattering [48]. This conclusion is supported by Hall effect measurements performed at RT (Table 1). The hole concentration increases monotonically with the Sn content and varies in the range 0.76 – 2.72×10^{20} cm^{-3}. The hole mobility μ_H is almost constant ~ 6.65 cm^2 V^{-1} s^{-1} up to x = 0.02. For higher Sn contents, μ_H is marginally reduced to ~ 3 cm^2 V^{-1} s^{-1} for x = 0.03 and x = 0.04, which is likely due to enhanced point-defect scattering in addition to possible intervalley scattering [24].

To further confirm band convergence and better explain the electronic transport properties, electronic band structure calculations have been performed for pristine TiCoSb, $TiCo_{0.85}Fe_{0.15}Sb$ and $TiCo_{0.85}Fe_{0.15}Sb_{0.97}Sn_{0.03}$ (Fig. 5). For TiCoSb, our previously predicted crystal structure was used [49]. Our first-principles calculations predict that pure TiCoSb has an indirect band gap of 1.05 eV (Fig. 5(a & d)). The valence band maximum (VBM) and conduction band minimum (CBM) are located at the Γ and X point of the BZ, respectively. The VBM at Γ has a small energy difference of 51 meV with the band edge at the L point, which is very close to that found in prior reports on TiCoSb [40, 41]. The valence bands show nearly parabolic dispersion around the high symmetry points. Thus, in *p*-type TiCoSb, band convergence is an effective approach to enhance the TE performance due to the bands lying at distant *k* points, a situation that lowers the detrimental role played by inter-band scattering compared to band convergence achieved at a single *k* point [50]. Substituting Fe for Co shifts the VBM (V1) from the heavy valence band at Γ to the light valence band at L (V2), which remains unaffected upon Sn doping, as illustrated in Fig. 5(b & e)

and Fig. 5(c & f), respectively. This shift supports the fact that the density-of-states effective mass will be greater for $TiCo_{0.85}Fe_{0.15}Sb_{0.97}Sn_{0.03}$ compared to $TiCo_{0.85}Fe_{0.15}Sb$ and TiCoSb. Further, the energy difference between V1 and V2 significantly decreases from 51 meV in TiCoSb to 10 meV in $TiCo_{0.85}Fe_{0.15}Sb$ and eventually to 5 meV in $TiCo_{0.85}Fe_{0.15}Sb_{0.97}Sn_{0.03}$. Therefore, the bands at Γ and L for Fe- and Sn-substituted samples are expected to contribute to transport near or below room temperature, while band convergence will only occur at ~ 600 K in pristine TiCoSb. Our calculations indicate that TiCoSb exhibits m^*_{DOS} of 4.0 m_e that increases to 5.0 m_e for $TiCo_{0.85}Fe_{0.15}Sb$ and to 7.9m_e for $TiCo_{0.85}Fe_{0.15}Sb_{0.97}Sn_{0.03}$. Although these values are slightly higher than those inferred from the experimental Seebeck coefficient values, these predictions are nevertheless in line with our experimental results and show that m^*_{DOS} increases due to the decreased energy offset between the valence band maxima. Moreover, the total and partial densities of states of the three compositions TiCoSb, $TiCo_{0.85}Fe_{0.15}Sb$, and $TiCo_{0.85}Fe_{0.15}Sb_{0.97}Sn_{0.03}$, shown in Fig. 5(g - i), confirm the significant shift of the Fermi level deeper into the valence bands and the impact of Fe on the density of states. Further, the substitution of Sn for Sb marginally modifies the density of states and the position of the Fermi level.

The power factor (*PF*), shown in Fig. 6(a), increases monotonically up to $x = 0.03$ for which an optimum value of ~1.94 mW m^{-1} K^{-2} is reached at 825 K. This peak value is comparable to that obtained in metallic, single-crystalline TiCoSb [40] and in optimized HHs at high temperatures [18, 51].

As another indicator of the effect of band convergence on the electronic properties, the temperature-dependent weighted mobility μ^* was calculated for each sample (Fig. 6(b)) from the temperature dependence of the electrical conductivity and Seebeck coefficient [52]

$$\mu^* = \frac{3h^3\sigma}{8\pi e(2m_e k_B T)^{3/2}}\left[\frac{exp\left[\frac{|\alpha|}{k_B/e} - 2\right]}{1 + exp\left[-5\left(\frac{|\alpha|}{k_B/e} - 1\right)\right]} + \frac{\frac{3}{\pi^2}\frac{|\alpha|}{k_B/e}}{1 + exp\left[5\left(\frac{|\alpha|}{k_B/e} - 1\right)\right]}\right]$$

As μ^* is a function of both m^*_{DOS} and the mobility of the charge carriers, the observed increase at RT upon doping evidences the direct benefit of band convergence on the electronic properties. At RT, the x = 0.03 sample has the highest weighted mobility ~ 41.6 $cm^2\ V^{-1}\ s^{-1}$, which corresponds to ~100 % improvement over the value of the Sn-free sample. The μ^* of all samples increases continuously with temperature up to a maximum value of ~ 65 $cm^2\ V^{-1}\ s^{-1}$ at ~580 K achieved for the x = 0.03 sample. The reduction observed at high temperatures may be due to thermally-activated conductivity at grain boundaries [53].

The temperature dependence of the total thermal conductivity κ for all samples $TiCo_{0.85}Fe_{0.15}Sb_{1-x}Sn_x$ ($0 \leq x \leq 0.04$) is shown in Fig. 7. The κ was calculated using the equation $\kappa = D \times \rho \times C_p$, where D is the thermal diffusivity, ρ is the experimental mass density and C_p is the specific heat. κ decreases monotonically upon Sn doping up to x = 0.03, before eventually increasing for x = 0.04 (Fig. 7(a)). This distinct behavior of κ for this last sample contrasts with the monotonic decrease in κ observed in earlier reports of TiCoSb [10, 54, 55]. This difference might be tied to the presence of Fe that leads to a shrinkage of the unit cell volume (a = 5.8897 Å for TiCoSb and a = 5.8854 Å for $TiCo_{0.85}Fe_{0.15}Sb$), thereby affecting the solubility limit of Sn in TiCoSb, or, alternatively, modifying the concentration of Fe in the HH matrix. In such a case, the actual chemical composition may differ from the nominal one, resulting in a departure from the observed monotonic trend in the transport properties with x up to x = 0.03. Such a distinct trend in κ with elemental doping has also been observed in earlier studies on TiCoSb [10, 54, 55]. For all samples, κ decreases continuously with temperature across the entire temperature range,

confirming the increased scattering of phonons at high temperatures. The lowest κ value of ~ 4.24 W $m^{-1} K^{-1}$ is achieved at ~ 874 K for the composition $TiCo_{0.85}Fe_{0.15}Sb_{0.97}Sn_{0.03}$. The lattice thermal conductivity κ_L, shown in Fig. 7(b), was calculated by subtracting the electronic thermal conductivity κ_e using the Wiedemann-Franz law $\kappa_e = L\sigma T$, where L is the Lorenz number. The L values were estimated by the relation $L = 1.5 + \exp(-|\alpha|/116)$ with L and α expressed in 10^{-8} $W\Omega K^{-2}$ and $\mu V\ K^{-1}$, respectively [56]. κ_L decreases monotonically with x up to $x = 0.03$ due to enhanced phonon scattering by the defects at various length scales evidenced by FESEM and HRTEM analysis. The κ_L values decrease continuously with increasing temperature for all samples, following a $T^{-0.5}$ law, suggesting that alloy scattering contributes to limit the thermal transport in these samples.

Fig. 8 shows the figure of merit *ZT* as a function of temperature. The *ZT* values are enhanced upon Sn doping due to the combined effect of improved power factor and reduced lattice thermal conductivity. A peak *ZT* value of ~0.4 at ~873 K was achieved in the $TiCo_{0.85}Fe_{0.15}Sb_{0.97}Sn_{0.03}$ sample, which is ~110 % higher than that of its pristine counterpart $TiCo_{0.85}Fe_{0.15}Sb$ and higher than those obtained in prior studies on Sn-doped TiCoSb [17, 57]. The comparison of this peak *ZT* value with those reported for TiCoSb-based compounds in prior studies (Table 2), shows that the value achieved herein is among the highest values reported for *p*-type TiCoSb alloys. In spite of numerous experimental investigations on both *n*- and *p*-type alloys, the thermoelectric performance achieved in the latter remains moderate.

Mechanical Properties

For integration into TE devices, good mechanical properties are a prerequisite to ensure the mechanical integrity of the TE legs. Therefore, the micro-hardness and fracture toughness of all

the synthesized samples were determined (Fig. S-2 in (*SI*)). The fracture toughness of all the samples was calculated by using a simple equation of half-penny model [58] based on Vickers indentation, $K_c = 0.0752\frac{P}{c^{3/2}}$. Here, K_c is the fracture toughness, *c* is the average length of cracks from the center of indentation, and *P* is the load of the indenter. The substitution of Sn for Sb does not significantly affect the mechanical properties. For all the samples, the micro-hardness remains in the range 7.9 – 8.8 GPa, which is comparable to the values measured in prior reports on TiCoSb [12, 59]. The observed micro-hardness values are much higher than that of the commercial materials (Bi_2Te_3, PbTe) and are close to the values reported for other HH alloys [60, 61]. Similarly, the fracture toughness of all samples was found to be in the range 1.7 – 2.2 MPa-$m^{-1/2}$, which are very close to those reported for HH alloys [12, 61].

4. Conclusion

In summary, we have shown that band convergence is a promising approach to improve the TE performance in the *p*-type TiCoSb half-Heusler alloy. Substituting Sn for Sb with 15 atom% Fe-doping in TiCoSb reduces the energy difference of 51 meV between the two valence bands located at the L and Γ points of the Brillouin zone, as demonstrated by electronic band structure calculations and analysis of the weighed mobility. Consequently, both the hole concentration and Seebeck coefficient increase upon Sn doping. The optimum Sn content of $x = 0.03$ yields an enhanced power factor of ~ 1.9 mW m^{-1} K^{-2} around 850 K. The increased disorder in the unit cell induced by these substitutions enhances point-defect scattering, thereby resulting in a significant reduction in the lattice thermal conductivity down to ~ 4.2 W m^{-1} K^{-1} at ~ 873 K in the composition $TiCo_{0.85}Fe_{0.15}Sb_{0.97}Sn_{0.03}$. The combination of improved power factor and lowered thermal conductivity leads to a maximum *ZT* value of ~ 0.4 at 873 K for $TiCo_{0.85}Fe_{0.15}Sb_{0.97}Sn_{0.03}$. The measured mechanical properties for all samples are comparable to those of TiCoSb, showing that

Fe and Sn co-doping has no detrimental influence on the mechanical properties. Further experimental studies should be carried out to improve the hole mobility and bring the performance of *p*-type alloys closer to those of their *n*-type analogues.

Supporting Information

Rietveld refinement data of $TiCo_{0.85}Fe_{0.15}Sb_{1-x}Sn_x$ along with the relative densities; linear fitting of Seebeck coefficient in temperature range from ~723 to ~870 K of all samples $TiCo_{0.85}Fe_{0.15}Sb_{1-x}Sn_x$; mechanical properties (micro-hardness and fracture toughness) of all samples $TiCo_{0.85}Fe_{0.15}Sb_{1-x}Sn_x$.

Acknowledgments

The authors would like to express their gratitude to Director, CSIR-NPL, New Delhi, India for his encouragement and support. AKV would like to express its gratitude for the financial support provided by UGC-India. KKJ wishes to express gratitude for the financial support offered by CSIR-India. DKS thanks to SERB for providing financial support vide letter no. PDF/2020/002789 Additionally, we appreciate the technical assistance provided by Mr. Radhey Shyam and Dr. Naval Kishor Upadhyay. We acknowledge Dr. J.S. Tawale for the FESEM and EDS measurements. We highly acknowledge Dr. Jasa Ram, DRDO, Defense Laboratory, Jodhpur, India for the thermal diffusivity measurements. The authors are thankful to Mr. Abhishek for plagiarism check utilizing the software iThenticate available in the library of CSIR-NPL, New Delhi, India.

Author's contribution

Ajay Kumar Verma: Synthesis, Methodology, data curation, formal analysis and original drafting of the manuscript

Kishor Kumar Johari: Methodology and formal analysis

Paritosh Dubey: HRTEM measurement and review

Durgesh Kumar Sharma: Theoretical analysis

Sudhir Kumar: Theoretical analysis

Sanjay R. Dhakate: Review, editing and supervision

Christophe Candolfi: Review, and editing

Bertrand Lenoir: Conceptualization, review, and editing

Bhasker Gahtori: Conceptualization, visualization, review, editing and supervision

Conflict of interest

The authors declare no conflict of interest.

Tables

Table 1: Room temperature Hall data for $TiCo_{0.85}Fe_{0.15}Sb_{1-x}Sn_x$.

Parameters	$x = 0$	$x = 0.01$	$x = 0.02$	$x = 0.03$	$x = 0.04$
Hole density (10^{20} cm^{-3})	0.76	0.96	1.16	2.47	2.72
Hall mobility (cm^2 V^{-1} s^{-1})	6.70	6.66	6.64	2.99	3.02
Hall coefficient (10^{-2} × cm^3/C)	8.20	6.52	5.38	2.53	2.30

Table 2: Comparison of the *ZT* values reported for *n*- and *p*-type TiCoSb-based HH compounds.

Composition/ Type	**Synthesis route**	**Peak *ZT***	**References**
$TiCoSb_{0.85}Ge_{0.15}$ / p-type	Arc melting + annealing at 1123 K for 7 days + SPS at 1223 K	~ 0.16 at 850 K	Ref.[14]
$TiCoSb_{0.8}Sn_{0.2}$/ p-type	Arc melting + SPS at 1473 K	~ 0.26 at 873 K	Ref.[62]

$TiCoSb_{0.9}Sn_{0.1}$/ p-type	Annealing at 1173 K for 7 days + SPS at 1373 K	~ 0.3 at 960 K	Ref.[57]
$TiCo_{0.5}Fe_{0.665}Sb$/ p-type	Arc melting + Annnealing at 1073 K for 9 days +ball milling for 6h + Hot press at 1223 K	~ 0.42 at 850 K	Ref.[63]
$TiCo_{0.85}Fe_{0.15}Sb$/ p-type	Arc melting + Annealing 1173 K for 24h + Annealing 1123 K for 7 days+ SPS at 1223 K	~ 0.45 at 850 K	Ref.[16]
$TiCoSb_{0.8}Sn_{0.2}$/ p-type	Arc melting + Annealing at 1173 K for 7 days	~ 0.5 at 973 K	Ref.[64]
$TiCo_{0.85}Fe_{0.15}Sb_{0.97}Sn_{0.03}$/ p-type	Arc melting + SPS at 1373 K	~ 0.4 at 873 K	Present work
TiCoSb / n-type	Arc melting + SPS at 1373 K	~ 0.02 at 823 K	Ref.[65]
$CoTi_{0.6}Nb_{0.2}Ta_{0.2}Sb_{0.2}Sn_{0.8}$/ n-type	Annealing at 1173 K for 60h + ball milling + Hot press at 1173 K	~ 0.08 at 936 K	Ref.[54]
$TiCo_{0.95}Pd_{0.05}Sb$/ n-type	Induction melting + SPS at 1323K	~ 0.1 at 823K	Ref.[66]
$Ti_{0.85}V_{0.15}CoSb$/ n-type	Arc melting + SPS at 1473 K	~0.22 at 873 K	Ref.[10]
$TiCo_{0.95}Ni_{0.05}Sb$/ n-type	Heating in argon at 1173K for 120 h+ SPS at 1123K	~0.27 at 900 K	Ref.[13]

$Ti_{0.92}Ta_{0.08}CoSb$/ n-type	Annealing at 1473 for 24h+ Annealing at 1133 K for 12 days + SPS at 1073 K	~0.3 at 900K	Ref.[19]
$TiCoNi_{0.1}Sb$/ n-type	Ball milling for 12h + SPS at 1073 K	~ 0.43 at 973 K	Ref.[67]
$Ti_{0.5}Zr_{0.25}Hf_{0.25}Co_{0.95}Ni_{0.05}Sb$/ n-type	Induaction melting + SPS at 1323 K	~ 0.51 at 813 K	Ref.[68]
$Ti_{0.85}Nb_{0.15}CoSb$/ n-type	Arc melting + SPS at 1473 K	~0.52 at 873 K	Ref.[10]
$Ti_{0.9}Ta_{0.1}CoSb$/ n-type	Arc melting + ball milling for 2h + SPS at 1373 K	~0.7 at 973 K	Ref.[18]
$Ti_{0.6}Hf_{0.4}Co_{0.87}Ni_{0.13}Sb$/ n-type	Arc melting + annealing at 1173 K for 7 days + SPS at 1423 K	~ 0.9 at 900 K	Ref.[55]

Figures

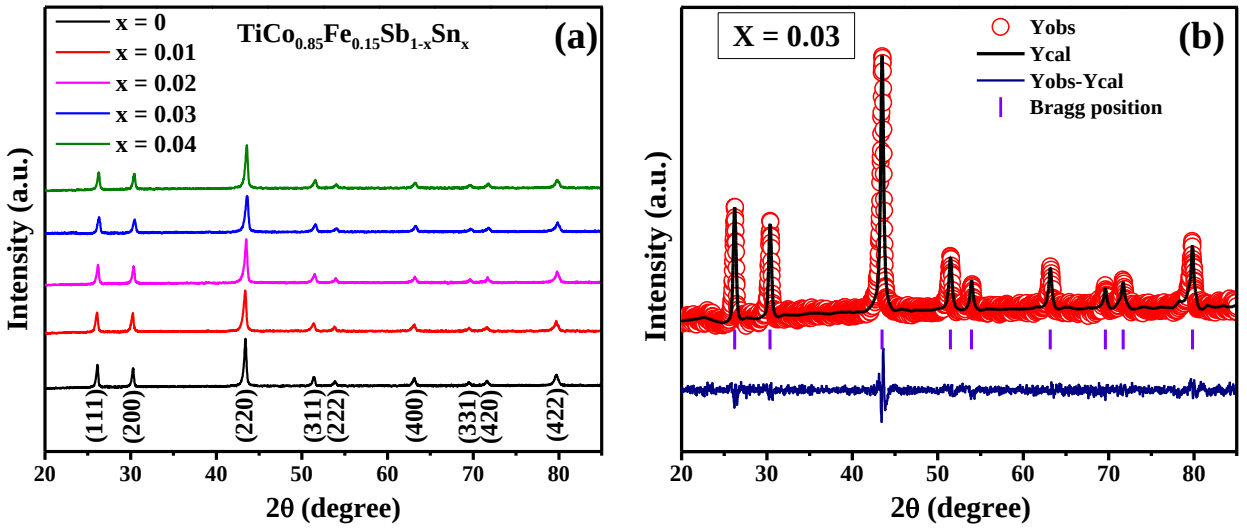

Fig. 1: (a) XRD patterns of the $TiCo_{0.85}Fe_{0.15}Sb_{1-x}Sn_x$ samples. (b) Rietveld refinement of the illustrative sample $TiCo_{0.85}Fe_{0.15}Sb_{0.97}Sn_{0.03}$.

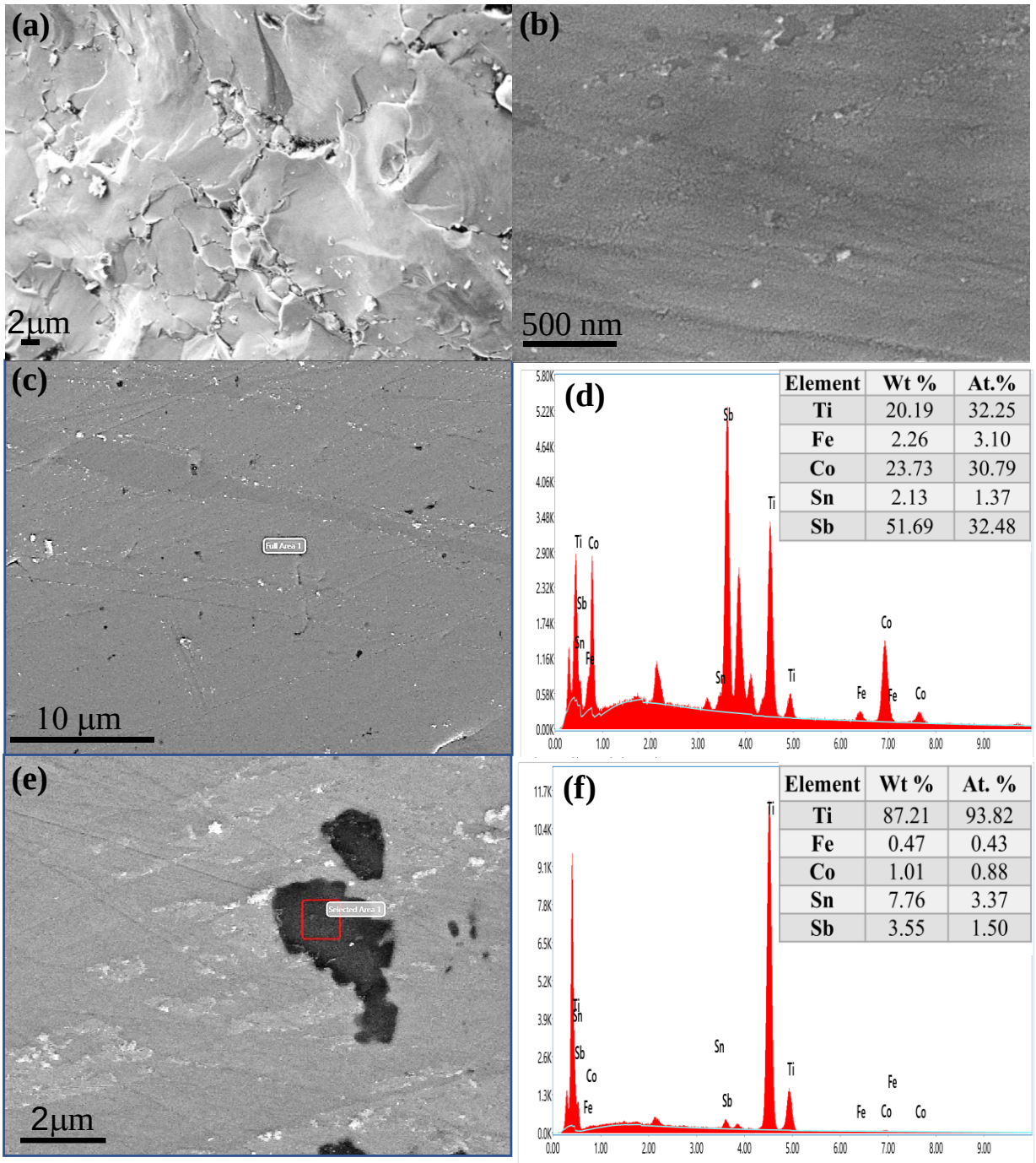

Fig. 2: FESEM and EDS analysis of $TiCo_{0.85}Fe_{0.15}Sb_{0.97}Sn_{0.03}$ sample: (a) fractured surface image, (b) magnified surface image, (c) Image of large area plain surface, (d) corresponding elemental composition, (e) magnified image with minor secondary phase, and (f) elemetal composition of minor secondary phase.

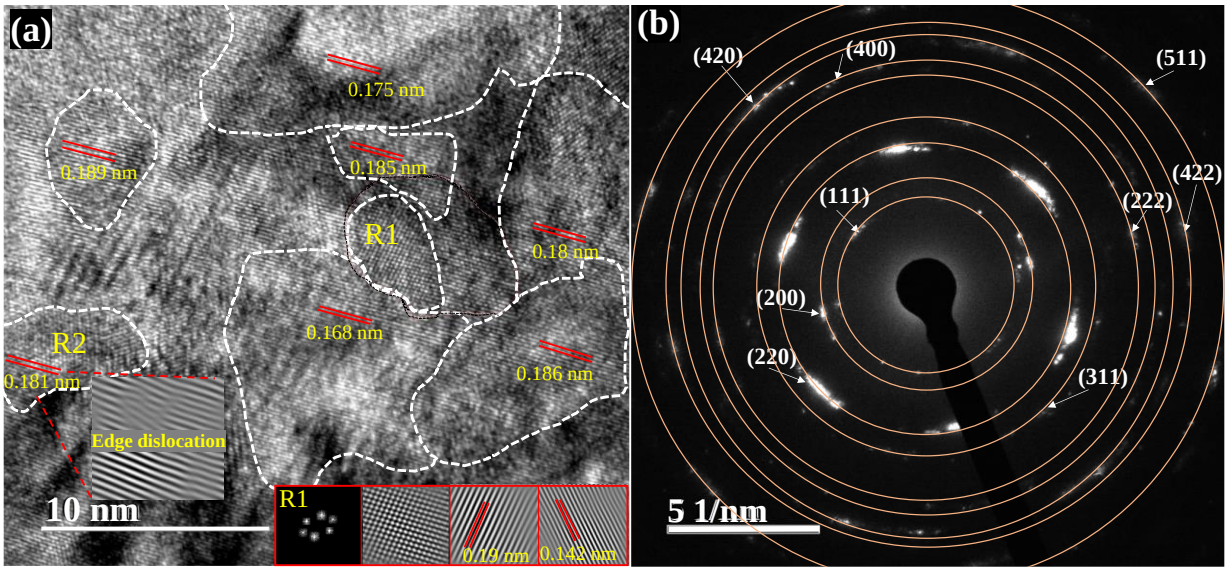

Fig. 3: (a) HRTEM image of $TiCo_{0.85}Fe_{0.15}Sb_{0.97}Sn_{0.03}$ sample, inset: Fast Fourier Transform (FFT) with planes of R1 region and magnified view of R2 region. (b) Selected area electron diffraction (SAED) pattern of corresponding Fig. 3(a).

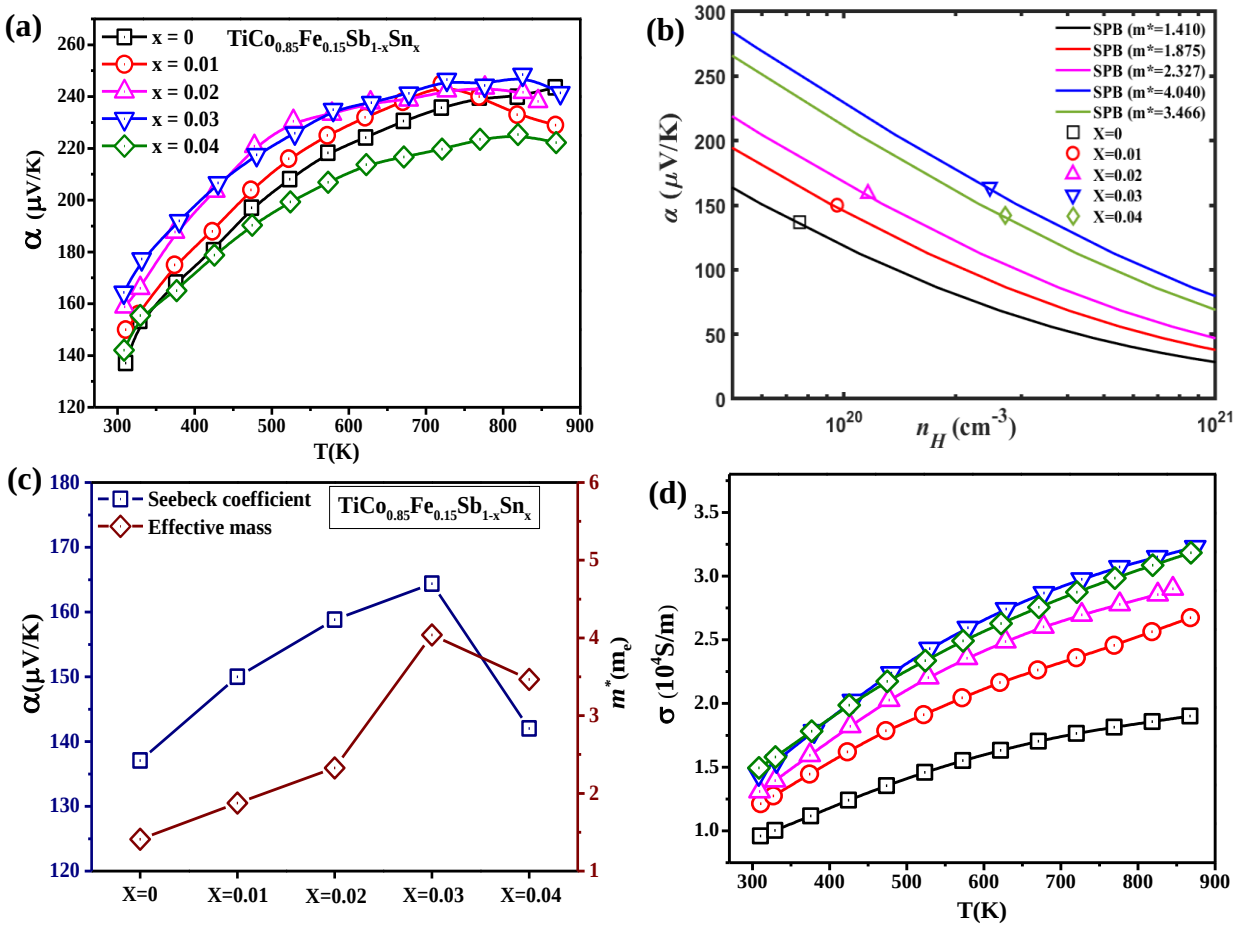

Fig. 4: (a) Temperature dependent Seebeck coefficient, (b) Ioffe-Pisarenko plot for $TiCo_{0.85}Fe_{0.15}Sb_{1-x}Sn_x$, where the solid lines were calculated by the SPB model, (c) compositional dependence of the Seebeck coefficient and density-of-states effective mass at RT, and (d) temperature dependence of the electrical conductivity.

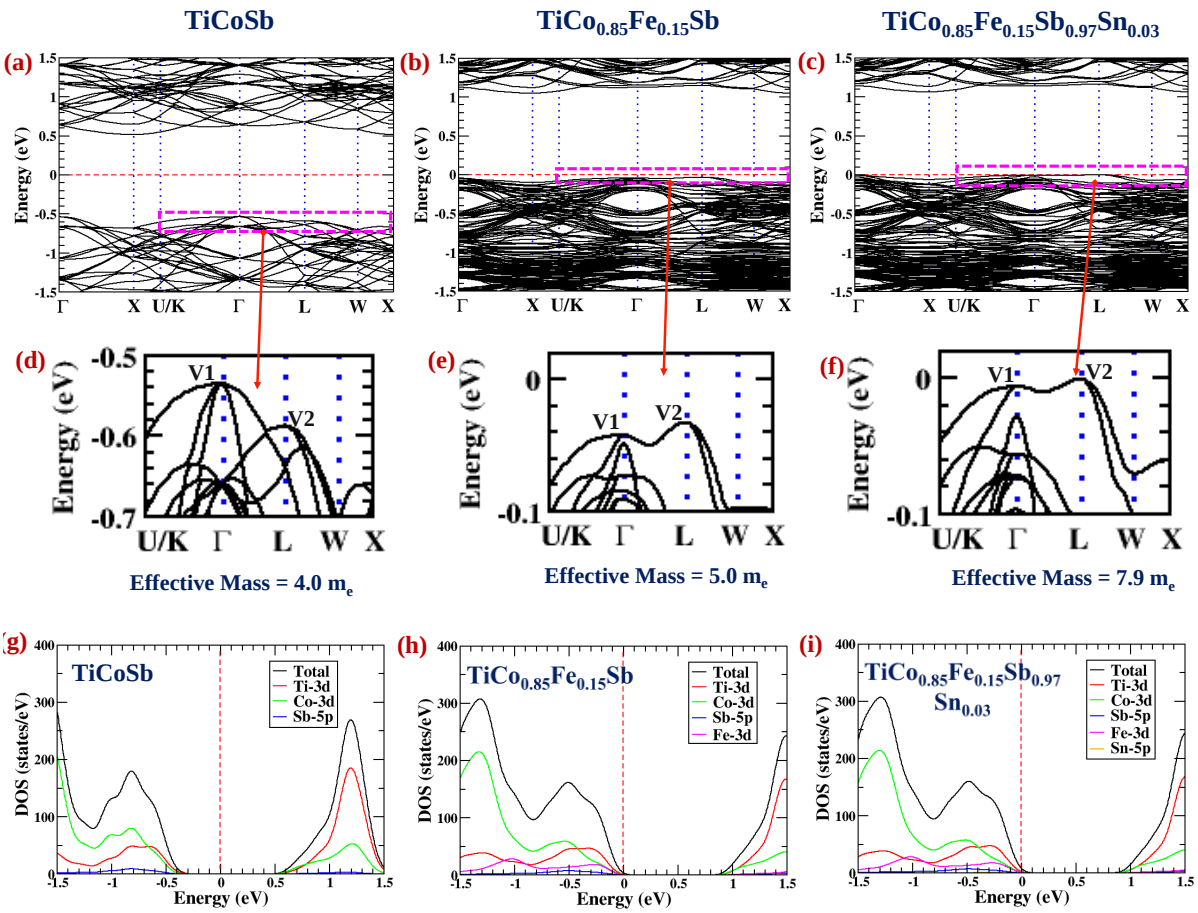

Fig. 5: Dispersion curves (a & d) of pristine TiCoSb, (b & e) of $TiCo_{0.85}Fe_{0.15}Sb$, and (c & f) of $TiCo_{0.85}Fe_{0.15}Sb_{0.97}Sn_{0.03}$. Energy dependence of the density of states of (g) TiCoSb, (h) $TiCo_{0.85}Fe_{0.15}Sb$, and (i) $TiCo_{0.85}Fe_{0.15}Sb_{0.97}Sn_{0.03}$.

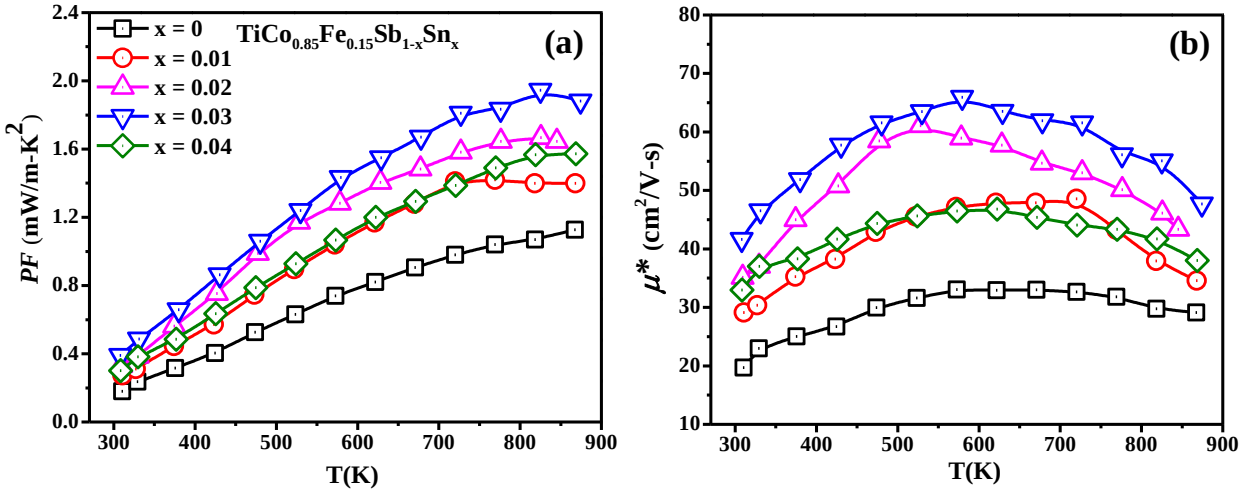

Fig. 6: Temperature dependent (a) power factor, and (b) weighted mobility, of $TiCo_{0.85}Fe_{0.15}Sb_{1-x}Sn_x$.

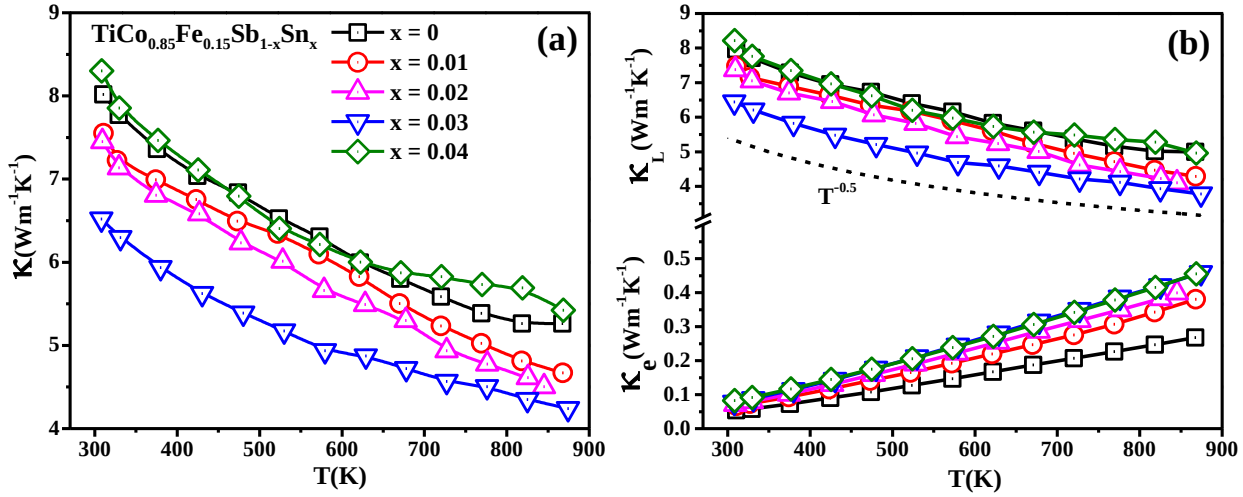

Fig. 7: (a) Total thermal conductivity and (b) electronic and lattice thermal conductivity as a function of temperature of the $TiCo_{0.85}Fe_{0.15}Sb_{1-x}Sn_x$ samples.

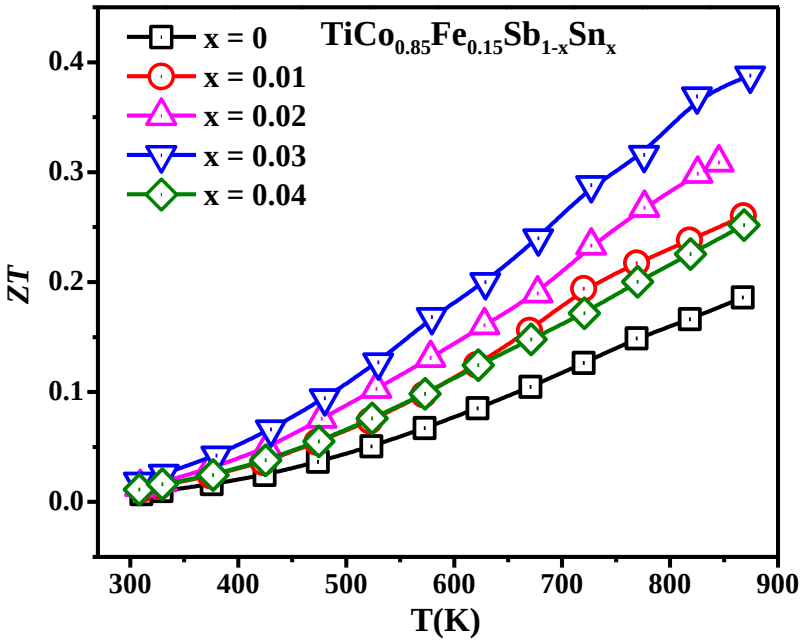

Fig. 8: Temperature dependence of the dimensionless thermoelectric figure of merit *ZT* of the $TiCo_{0.85}Fe_{0.15}Sb_{1-x}Sn_x$ samples.

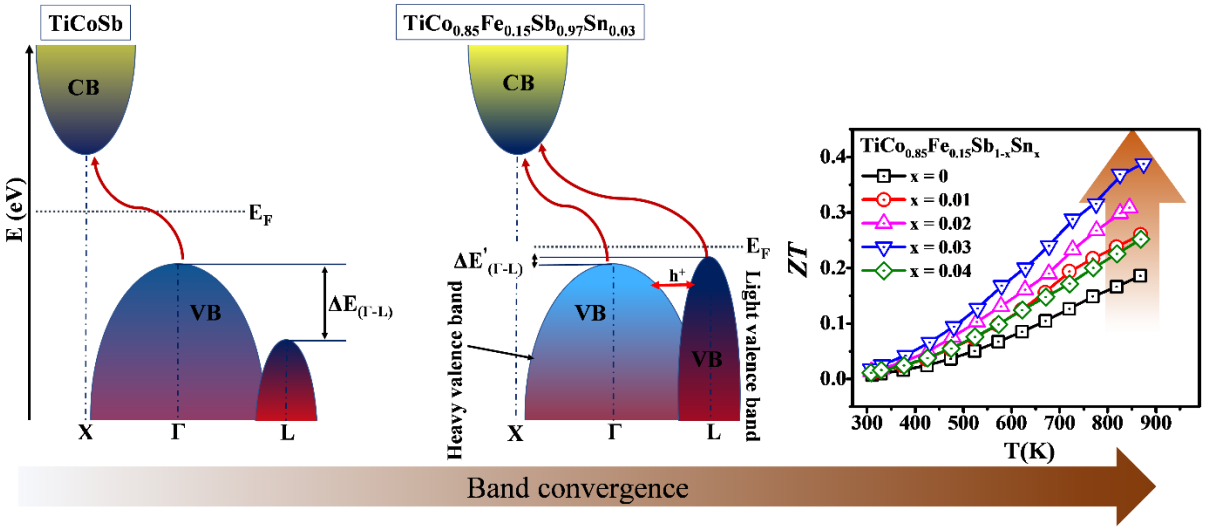

Graphical Abstract

References

1. Shi, X.-L., J. Zou, and Z.-G. Chen, *Advanced thermoelectric design: from materials and structures to devices.* Chemical Reviews, 2020. **120**(15): p. 7399-7515.
2. Fu, C., et al., *Band engineering of high performance p-type FeNbSb based half-Heusler thermoelectric materials for figure of merit zT> 1.* Energy & Environmental Science, 2015. **8**(1): p. 216-220.
3. Chauhan, N.S., et al., *Enhanced thermoelectric performance in p-type ZrCoSb based half-Heusler alloys employing nanostructuring and compositional modulation.* Journal of Materiomics, 2019. **5**(1): p. 94-102.
4. Berry, T., et al., *Enhancing thermoelectric performance of TiNiSn half-Heusler compounds via modulation doping.* Chemistry of Materials, 2017. **29**(16): p. 7042-7048.
5. Mallick, M.M. and S. Vitta, *Enhancing the thermoelectric performance of a p-type half-Heusler alloy, HfCoSb by incorporation of a band-matched chalcogenide, Cu 2 Te.* Journal of Materials Chemistry A, 2018. **6**(30): p. 14709-14716.
6. Shi, Y., C. Sturm, and H. Kleinke, *Chalcogenides as thermoelectric materials.* Journal of Solid State Chemistry, 2019. **270**: p. 273-279.
7. Rogl, G. and P. Rogl, *Skutterudites, a most promising group of thermoelectric materials.* Current opinion in green and sustainable chemistry, 2017. **4**: p. 50-57.
8. Tseng, Y.-C., et al., *Advancing the reliability of thermoelectric materials: A case study of silicides through statistics.* Applied Physics Letters, 2021. **119**(19): p. 193903.
9. Takabatake, T., et al., *Phonon-glass electron-crystal thermoelectric clathrates: Experiments and theory.* Reviews of Modern Physics, 2014. **86**(2): p. 669.
10. Vishwakarma, A., et al., *Compositional modulation is driven by aliovalent doping in n-type TiCoSb based half-Heuslers for tuning thermoelectric transport.* Intermetallics, 2020. **125**: p. 106914.
11. Johari, K.K., et al., *High Thermoelectric Performance in n-Type Degenerate ZrNiSn-Based Half-Heusler Alloys Driven by Enhanced Weighted Mobility and Lattice Anharmonicity.* ACS Applied Energy Materials, 2021. **4**(4): p. 3393-3403.
12. Verma, A.K., et al., *Role of sintering temperature on electronic and mechanical properties of thermoelectric material: A theoretical and experimental study of TiCoSb half-Heusler alloy.* Materials Chemistry and Physics, 2022: p. 125854.
13. Zhou, M., et al., *Effects of partial substitution of Co by Ni on the high-temperature thermoelectric properties of TiCoSb-based half-Heusler compounds.* Journal of alloys and compounds, 2005. **391**(1-2): p. 194-197.

14. Wu, T., et al., *Effects of Ge doping on the thermoelectric properties of TiCoSb-based p-type half-Heusler compounds.* Journal of alloys and compounds, 2009. **467**(1-2): p. 590-594.
15. Kuentzler, R., et al., *Gap at the Fermi level and magnetism in RMSn ternary compounds (R= Ti, Zr, Hf and M= Fe, Co, Ni).* Journal of Magnetism and Magnetic Materials, 1992. **104**: p. 1976-1978.
16. Wu, T., et al., *Thermoelectric properties of p-type Fe-doped TiCoSb half-Heusler compounds.* Journal of Applied Physics, 2007. **102**(10): p. 103705.
17. Sekimoto, T., et al., *Thermoelectric properties of Sn-doped TiCoSb half-Heusler compounds.* Journal of alloys and compounds, 2006. **407**(1-2): p. 326-329.
18. Wang, R.-F., et al., *Enhanced thermoelectric performance of n-type TiCoSb half-Heusler by Ta doping and Hf alloying.* Rare Metals, 2021. **40**(1): p. 40-47.
19. Zhou, M., et al., *Moderate-temperature thermoelectric properties of TiCoSb-based half-Heusler compounds Ti 1− x Ta x Co Sb.* Journal of applied physics, 2007. **101**(11): p. 113714.
20. Johari, K.K., et al., *In Situ Evolution of Secondary Metallic Phases in Off-Stoichiometric ZrNiSn for Enhanced Thermoelectric Performance.* ACS Applied Materials & Interfaces, 2022.
21. Yan, X., et al., *Thermoelectric Property Study of Nanostructured p-Type Half-Heuslers (Hf, Zr, Ti) CoSb0. 8Sn0. 2.* Advanced Energy Materials, 2013. **3**(9): p. 1195-1200.
22. Chauhan, N., et al., *A synergistic combination of atomic scale structural engineering and panoscopic approach in p-type ZrCoSb-based half-Heusler thermoelectric materials for achieving high ZT.* Journal of Materials Chemistry C, 2016. **4**(24): p. 5766-5778.
23. DiSalvo, F.J., *Thermoelectric cooling and power generation.* Science, 1999. **285**(5428): p. 703-706.
24. Pei, Y., et al., *Convergence of electronic bands for high performance bulk thermoelectrics.* Nature, 2011. **473**(7345): p. 66-69.
25. Mahan, G., *Solid state physics.* Academic Press, New York, 1998. **51**(81): p. 11.
26. Tan, G., L.-D. Zhao, and M.G. Kanatzidis, *Rationally designing high-performance bulk thermoelectric materials.* Chemical reviews, 2016. **116**(19): p. 12123-12149.
27. Xiao, Y. and L.-D. Zhao, *Charge and phonon transport in PbTe-based thermoelectric materials.* npj Quantum Materials, 2018. **3**(1): p. 1-12.
28. Tan, G., et al., *Valence band modification and high thermoelectric performance in SnTe heavily alloyed with MnTe.* Journal of the American Chemical Society, 2015. **137**(35): p. 11507-11516.
29. Tang, Y., et al., *Convergence of multi-valley bands as the electronic origin of high thermoelectric performance in CoSb3 skutterudites.* Nature materials, 2015. **14**(12): p. 1223-1228.
30. Liu, W., et al., *Convergence of conduction bands as a means of enhancing thermoelectric performance of n-type Mg 2 Si 1− x Sn x solid solutions.* Physical review letters, 2012. **108**(16): p. 166601.
31. Pang, H., et al., *Realizing ranged performance in SnTe through integrating bands convergence and DOS distortion.* Journal of Materiomics, 2022. **8**(1): p. 184-194.
32. Tan, G., et al., *Extraordinary role of Hg in enhancing the thermoelectric performance of p-type SnTe.* Energy & Environmental Science, 2015. **8**(1): p. 267-277.
33. T. Hung, N., et al., *Thermoelectric performance of monolayer InSe improved by convergence of multivalley bands.* Journal of Applied Physics, 2019. **125**(8): p. 082502.
34. Pei, J., et al., *Bi2Te3-based applied thermoelectric materials: research advances and new challenges.* National science review, 2020. **7**(12): p. 1856-1858.
35. Ryu, B., et al., *Prediction of the band structures of Bi2Te3-related binary and Sb/Se-doped ternary thermoelectric materials.* Journal of the Korean Physical Society, 2016. **68**(1): p. 115-120.
36. Brod, M.K. and G.J. Snyder, *Orbital chemistry of high valence band convergence and low-dimensional topology in PbTe.* Journal of Materials Chemistry A, 2021. **9**(20): p. 12119-12139.

37. Jood, P., et al., *Na doping in PbTe: solubility, band convergence, phase boundary mapping, and thermoelectric properties.* Journal of the American Chemical Society, 2020. **142**(36): p. 15464-15475.
38. Guo, S., et al., *Conduction band engineering of half-Heusler thermoelectrics using orbital chemistry.* Journal of Materials Chemistry A, 2022. **10**(6): p. 3051-3057.
39. Brod, M.K., S. Anand, and G.J. Snyder, *The Importance of Avoided Crossings in Understanding High Valley Degeneracy in Half-Heusler Thermoelectric Semiconductors.* Advanced Electronic Materials, 2022. **8**(4): p. 2101367.
40. Serrano-Sanchez, F., et al., *Electronic structure and low-temperature thermoelectric transport of TiCoSb single crystals.* Nanoscale, 2022.
41. Kumarasinghe, C. and N. Neophytou, *Band alignment and scattering considerations for enhancing the thermoelectric power factor of complex materials: The case of Co-based half-Heusler alloys.* Physical Review B, 2019. **99**(19): p. 195202.
42. Rodriguez-Carvajal, J., *FullProof Suite.* Physica B, 1993.
43. Zhao, D., et al., *Synthesis and thermoelectric properties of tantalum-doped ZrNiSn half-Heusler alloys.* Functional Materials Letters, 2014. **7**(03): p. 1450032.
44. Humbe, A.V., et al., *Rietveld refinement, morphology and superparamagnetism of nanocrystalline Ni0. 70− xCuxZn0. 30Fe2O4 spinel ferrite.* Ceramics International, 2018. **44**(5): p. 5466-5472.
45. May, A.F. and G.J. Snyder, *Introduction to modeling thermoelectric transport at high temperatures*, in *Materials, preparation, and characterization in thermoelectrics*. 2017, CRC press. p. 207-224.
46. Naithani, H. and T. Dasgupta, *Critical analysis of single band modeling of thermoelectric materials.* ACS Applied Energy Materials, 2019. **3**(3): p. 2200-2213.
47. D'Souza, R., et al., *Temperature Induced Band Convergence, Intervalley Scattering, and Thermoelectric Transport in p-Type PbTe.* ACS Applied Energy Materials, 2022.
48. Wiendlocha, B., et al., *Residual resistivity as an independent indicator of resonant levels in semiconductors.* Materials Horizons, 2021. **8**(6): p. 1735-1743.
49. Verma, A.K., et al., *Role of sintering temperature on electronic and mechanical properties of thermoelectric material: A theoretical and experimental study of TiCoSb half-Heusler alloy.* Materials Chemistry and Physics, 2022. **281**: p. 125854.
50. Park, J., et al., *When band convergence is not beneficial for thermoelectrics.* Nature communications, 2021. **12**(1): p. 1-8.
51. Zhu, H., et al., *Discovery of ZrCoBi based half Heuslers with high thermoelectric conversion efficiency.* Nature communications, 2018. **9**(1): p. 1-9.
52. Snyder, G.J., et al., *Weighted mobility.* Advanced Materials, 2020. **32**(25): p. 2001537.
53. Kuo, J.J., et al., *Grain boundary dominated charge transport in Mg 3 Sb 2-based compounds.* Energy & Environmental Science, 2018. **11**(2): p. 429-434.
54. Kawaharada, Y., et al., *High temperature thermoelectric properties of CoTiSb half-Heusler compounds.* Journal of alloys and compounds, 2004. **384**(1-2): p. 308-311.
55. Qiu, P., et al., *Enhanced thermoelectric performance by the combination of alloying and doping in TiCoSb-based half-Heusler compounds.* Journal of Applied Physics, 2009. **106**(10): p. 103703.
56. Kim, H.-S., et al., *Characterization of Lorenz number with Seebeck coefficient measurement.* APL materials, 2015. **3**(4): p. 041506.
57. Sekimoto, T., et al. *Thermoelectric properties of (Ti, Zr) CoSnxSb1-x half-Heusler compounds*. in *2006 25th International Conference on Thermoelectrics*. 2006. IEEE.
58. Moradkhani, A., et al., *Determination of fracture toughness using the area of micro-crack tracks left in brittle materials by Vickers indentation test.* Journal of Advanced Ceramics, 2013. **2**(1): p. 87-102.

59. Rogl, G., et al., *Mechanical properties of half-Heusler alloys.* Acta Materialia, 2016. **107**: p. 178-195.
60. He, R., et al., *Studies on mechanical properties of thermoelectric materials by nanoindentation.* physica status solidi (a), 2015. **212**(10): p. 2191-2195.
61. O'Connor, C.J., *Nanostructured Composite Materials for High Temperature Thermoelectric Energy Conversion*. 2012, NEW ORLEANS UNIV LA.
62. Chauhan, N.S., et al., *Enhanced thermoelectric performance in Hf-Free p-type (Ti, Zr) CoSb half-heusler alloys.* Journal of Electronic Materials, 2019. **48**(10): p. 6700-6709.
63. Tavassoli, A., et al., *The half Heusler system Ti 1+ x Fe 1.33− x Sb–TiCoSb with Sb/Sn substitution: phase relations, crystal structures and thermoelectric properties.* Dalton Transactions, 2018. **47**(3): p. 879-897.
64. Rausch, E., et al., *Enhanced thermoelectric performance in the p-type half-Heusler (Ti/Zr/Hf) CoSb 0.8 Sn 0.2 system via phase separation.* Physical Chemistry Chemical Physics, 2014. **16**(46): p. 25258-25262.
65. Sekimoto, T., et al. *Thermoelectric and thermophysical properties of TiCoSb, ZrCoSb, HfCoSb prepared by SPS*. in *ICT 2005. 24th International Conference on Thermoelectrics, 2005.* 2005. IEEE.
66. Xie, W., et al., *Synthesis and thermoelectric properties of (Ti, Zr, Hf)(Co, Pd) Sb half-Heusler compounds.* Journal of Physics D: Applied Physics, 2009. **42**(23): p. 235407.
67. Liu, L., et al., *Interfacial Decoration Tailoring the Thermoelectric Performance of TiCoNi x Sb Half-Heusler Compounds.* ACS Applied Energy Materials, 2021. **4**(7): p. 7148-7156.
68. Xie, W., Q. Jin, and X. Tang, *The preparation and thermoelectric properties of Ti 0.5 Zr 0.25 Hf 0.25 Co 1− x Ni x Sb half-Heusler compounds.* Journal of applied physics, 2008. **103**(4): p. 043711.

Supporting Information

Realization of Band Convergence in p-Type TiCoSb Half-Heusler Alloy Significantly Enhances the Thermoelectric Performance

Ajay Kumar Verma[1, 2, 3, 4], Kishor Kumar Johari[1, 2], Paritosh Dubey[2, 5], Durgesh Kumar Sharma[6,7], Sudhir Kumar[7], Sanjay Rangnate Dhakate [1, 2], Christophe Candolfi[8], Bertrand Lenoir[8 *], and Bhasker Gahtori[1, 2, *]

[1]*CSIR-National Physical Laboratory, Dr. K.S. Krishnan Marg, New Delhi-110012, India*
[2]*Academy of Scientific & Innovative Research (AcSIR), Ghaziabad-201002, India*
[3]*Functional Materials and Microsystems Research Group and the Micro Nano Research Facility, RMIT University, Melbourne, VIC 3001, Australia*
[4]*School of Engineering, RMIT University, GPO Box 2476, Melbourne, Victoria 3001, Australia*
[5]*CSIR-National Metallurgical Laboratory, Jamshedpur 831007, India*
[6]*Present Address: Theoretical Sciences Unit, Jawaharlal Nehru Centre for Advanced Scientific Research, Jakkur, Bangalore - 560064, India.*
[7]*Applied Physics Department, Faculty of Engineering and Technology, M. J. P. Rohilkhand University, Bareilly - 243006, India*
[8]*Institut Jean Lamour UMR 7198 CNRS – Université de Lorraine Campus ARTEM, 2 allée André Guinier, BP 50840, Nancy 54011, France*

Table S-1: Rietveld refinement data for $TiCo_{0.85}Fe_{0.15}Sb_{1-x}Sn_x$ along with the relative densities of samples.

Sample Details	R_p	R_{wp}	R_e	χ^2	*a* (Å)	Relative Density (%)
***x* = 0**	39.0	24.3	12.5	3.776	5.8854	~ 97
***x* = 0.01**	32.7	22.5	11.9	3.595	5.8814	~ 93
***x* = 0.02**	38.1	24.5	12.5	3.854	5.8802	~ 96
***x* = 0.03**	33.8	23.5	12.2	3.706	5.8857	~ 97
***x* = 0.04**	37.9	24.1	12.9	3.472	5.8865	~ 97

*Corresponding authors: bhasker@nplindia.org, bertrand.lenoir@univ-lorraine.fr
Tel.: +91-11-45608556; Fax: +91-11-45609310

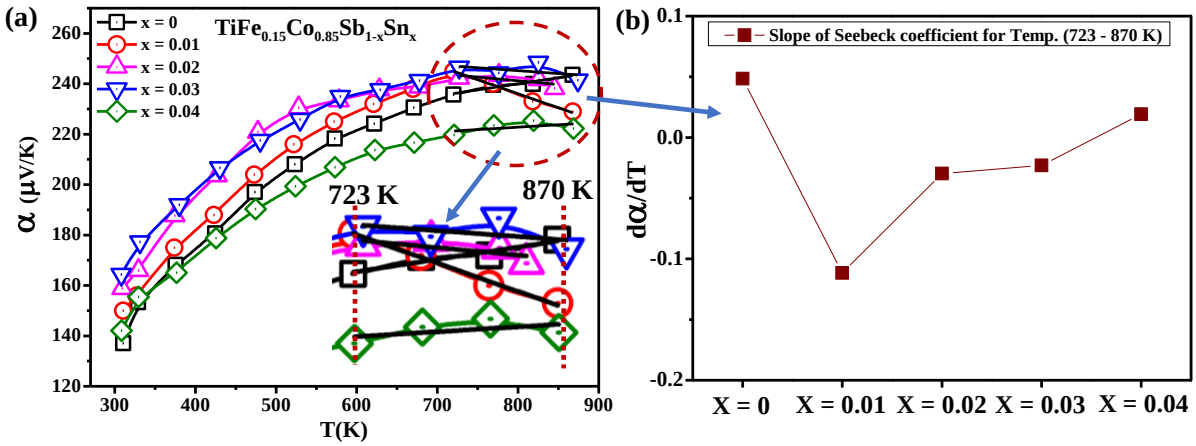

Fig. S-1: (a) linear fitting of Seebeck coefficient in temperature range from ~723 to ~870 K, and (b) change in Seebeck slope with Sn concentration.

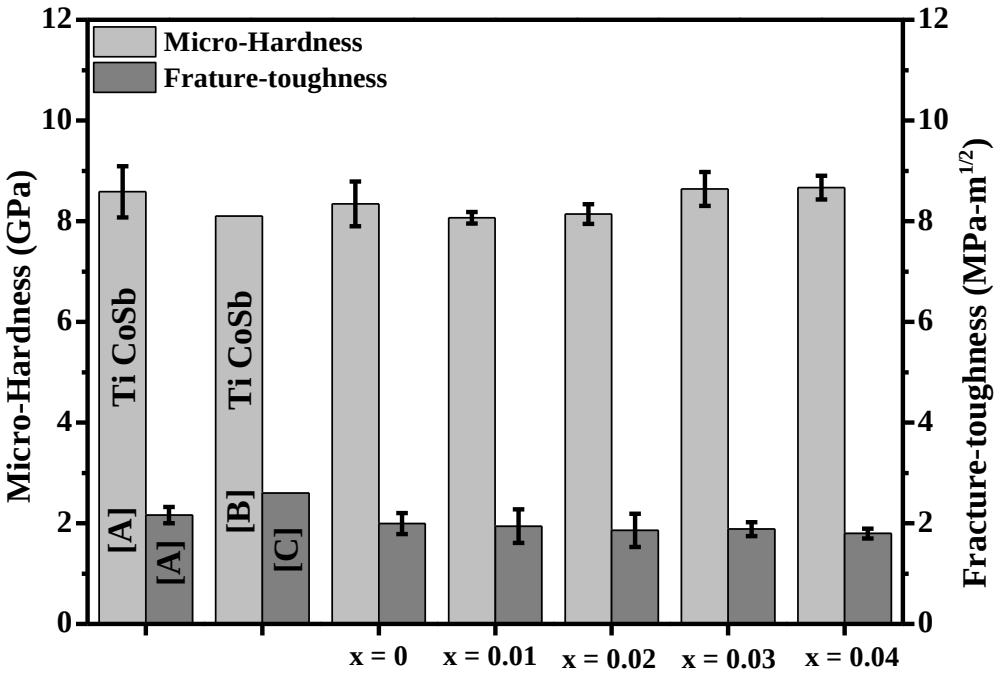

Fig. S-2: Mechanical properties (micro-hardness and fracture toughness) of the $TiCo_{0.85}Fe_{0.15}Sb_{1-x}Sn_x$ samples. For comparison, literature data have been added ([A][1], [B][2] and [C][3]).

References:

(1) Verma, A. K.; Johari, K. K.; Tyagi, K.; Sharma, D. K.; Kumar, P.; Kumar, S.; Bathula, S.; Dhakate, S.; Gahtori, B. Role of sintering temperature on electronic and mechanical properties of thermoelectric material: A theoretical and experimental study of TiCoSb half-Heusler alloy. *Materials Chemistry and Physics* **2022**, 125854.
(2) Rogl, G.; Grytsiv, A.; Gürth, M.; Tavassoli, A.; Ebner, C.; Wünschek, A.; Puchegger, S.; Soprunyuk, V.; Schranz, W.; Bauer, E. Mechanical properties of half-Heusler alloys. *Acta Materialia* **2016**, *107*, 178-195.
(3) O'Connor, C. J. *Nanostructured Composite Materials for High Temperature Thermoelectric Energy Conversion*; NEW ORLEANS UNIV LA, 2012.